Validation of a mid-fidelity CFD/CSD coupling using the Lattice-Boltzmann Method

Bastian Horvat * Ilkay Yavrucuk †

Institute for Helicopter Technology and VTOL
Technical University of Munich, 80333 Munich, Germany

In this study, a mid-fidelity tightly coupled CFD/CSD framework using a Lattice-Boltzmann method fluid solver is validated against experimental rotor measurements conducted during hover and wind tunnel conditions. The study also includes UH60A rotor measurements in both wind tunnel and flight conditions. The rotor is simulated using two diferrent actuator disk approaches and an actuator line model. Furthermore, an internal Peters-He inflow model is used as a reference for validation. All inflow models are evaluated for their ability to predict rotor power, load distribution, blade motion and control input. The results indicate that all models have deficiencies in power prediction for the experimental rotor. Hover and wind tunnel blade load variations show good agreement. Results for the UH60A rotor are consistent with power estimates, blade flap, and control input. The framework is capable of simulating rotors, but the accuracy of power prediction depends on rotor geometry and is strongly affected by the treatment of blade tips in load computation.

Nomenclature

β	blade flap angle
ε	kernel width
η_{ij}	kernel function for i-th blade and j-th blade element
μ	advance ratio
ψ	azimuth angle
Θ_0	mean blade pitch input
$\Theta_{1,c}$	first harmonic cosine blade pitch
$\Theta_{1,s}$	first harmonic sine blade pitch
b_Δ	blade element width
$C_{\mathrm{TL},\%}$	tip loss in percent
C_{TL}	tip loss factor
C_Q	torque coefficient
C_T	thrust coefficient
J_i	i-th Bessel function
j_i	i-th bessel root
l	tip loss parameter
N_{Cell}	number of fluid cells intersected by rotor
N_{be}	number of blade elements per blade
N_{blades}	number of rotor blades
$N_{\mathrm{h},\Psi}$	number of harmonics in azimuth direction
N_{r}	number of bessel functions in radial direction
p_N	distance between cell and blade element perpendicular to blade span
R	rotor radius
r	radial position
r_D	distance between fluid cell and blade element
T	thrust
$t_{i,c}$	i-th thrust series cosine coefficient
$t_{i,s}$	i-th thrust series sine coefficient
$t_{ij,c}$	thrust cosine coefficient for i-th bessel root and j-th harmonic
$t_{ij,s}$	thrust sine coefficient for i-th bessel root and j-th harmonic
t_{ij}	thrust of i-th blade and j-th blade element
u_i	velocity in i-direction
u_{i0}	mean velocitiy component in i-direction
u_{ic}	cosine velocitiy coefficient in i-direction

* Graduate Research Assistant, b.horvat@tum.de
† Professor and Head of Institute, ilkay.yavrucuk@tum.de

Presented at the 49th European Rotorcraft Forum, Bueckeburg, Germany, 2023

u_{is} sin velocitiy coefficient in i-direction

v_i rotor inflow velocity

1 Introduction

The rotorcraft research community still seeks to model complex scenarios where the rotorcraft faces challenges such as air wakes from ships, rotor-rotor interactions, or flight in close proximity to obstructions such as landing platforms or walls. Computational models and codes have been developed over time to address these situations. A low-cost and low-fidelity approach are finite-state inflow models that have the capability to account for free stream flow conditions through superposition or rotor-rotor interation through interference models, as demonstrated in Ref. [1]. However, their accuracy in complex flow environments may be severely limited. Particle or wake methods are a mid-level approach that offers the capability to model rotor-rotor interaction. However, they face challenges with arbitrary obstructions and non-uniform ambient flow conditions.

Three-dimensional computational fluid dynamics (CFD) methods, such as finite-volume or finite-differences, represent a high-fidelity solution that can provide detailed insight into rotor aerodynamics. However, they often come with a high computational cost and run time, making them challenging to use productively for iterative processes or under varying mission conditions. To address this issue, modeling the rotor with a simplified approach, rather than blade-resolved simulations, can significantly reduce costs. This simplification often involves using either an actuator disk (AD) or an actuator line (ACL) model in the CFD simulation of the flow surrounding the rotor. In the AD model, the rotor is represented as a continuous source term distribution over the entire rotor area. This leads to the loss of information about the tip vortices, but the downwash effect of the rotor is still simulated. Contrary to that, the ACL model presents the blade forces as source terms at the current blade position, providing a more detailed understanding of the wake evolution, including tip vortices.

Both approaches are used in the research community for simulating wind turbines and rotorcrafts. Sörensen et al. demonstrated the usage of AD in wind turbine simulations (Ref. [2]). Lechuiton et al. used AD to estimate the download of rotor downwash on the fuselage of a rotorcraft (Ref. [3]). Barakos et al. (Ref. [4]) presented various methods to estimate the circulation distribution across the disk for different flight conditions based on theoretical considerations. In recent publication, Ahmad et al. (Ref. [5]) used an AD model for a coaxial configuration to estimate the download on the fuselage, while Chiew et al. (Ref. [6]) simulated multicopter wakes using an AD model to predict lift and drag for a quadcopter. The ACL approach is widely used for simulating rotors, particularly in the wind turbine industry. Extensive research has been conducted and is ongoing in regards to inflow sampling, accounting for shed and bound vorticity in the inflow computation, and the source term distribution of blade forces in flow simulation. Jha et al. (Ref. [7]) provide a detailed overview of the current state of the art for ACL modeling and suggest guidelines.

This simplified modeling of rotors enhances computing efficiency by using lower resolutions compared to blade-resolved simulations. Nonetheless, computational time may still be considerable. To boost computing speed further, one can solve the flow equations with a Lattice-Boltzmann method (LBM) based fluid solver instead of more commonly used methods like finite volume or finite differences. The LBM solves the Navier-Stokes equations using particle distribution functions instead of macroscopic quantities like velocity or density. The formulation for these particles' interactions allow for a highly parallelized solver that is well suited for GPUs. This approach results in high computational speeds and enables the accurate capture of complex flow conditions in the three-dimensional flow field, making it an attractive option for mid-fidelity rotor modeling with AD or ACL methods.

Past studies in this field encompassed Friedman et al. (Ref. [8]) who utilized LBM in the real-time simulation of rotorcraft downwash with an AD model and no coupling with flight dynamics, specifically for real-time computation in the vicinity of arbitrary obstacles. Bludau et al. (Ref. [9]) coupled the LBM framework with a flight dynamics model by using the LBM flow solution as inflow, demonstrating its real-time capability. Bludau et al. (Ref. [10]) compared results with flight test data of a Bo105. The results were in good agreement and supported the continued advancement of the LBM/flight dynamics framework. Horvat et al. (Ref. [11]) expanded the framework by coupling the fluid simulation domain with an external flow field. This extension was utilized in examining flight and hover operations in a wind farm (Ref. [12]). Bludau et al. (Ref. [13]) applied the framework to a simple ship deck landing maneuver.

The presented work validates the mid-fidelity coupling of a CFD/CSD between the LBM-based fluid solver and Dymore, a multi-body structural dynamics solver (Ref. [14]).To reduce complexity, the study concentrates on an experimental teetering rotor operating in hover (Ref. [15]) and in wind tunnel conditions (Ref. [16]), and does not model a full rotorcraft in flight. Additionally, the framework is compared to wind tunnel and flight test data for the UH60A rotor. The rotor is modeled as an AD or ACL in the flow simulation. Blade forces are computed using velocities extracted from the flow field and then applied to blade element theory in the structural code. The purpose of this study is to evaluate the effectiveness of the LBM framework with rotor models of either AD or ACL in predicting experimental measurements such as C_P, blade motion, and required control input for both an experimental and a rotor in operational use.

The paper introduces a new set of basis functions for AD coupling and applies AD and AL models to LBM-based rotor simulations. While AD and ACL methods are not new, their application on a strictly Cartesian grid (due to LBM) presents a new challenge that the paper addresses. The results will also increase the understanding if and where the LBM can serve as a means to simulate complex rotorcraft scenarios in contrast to low-fidelity methods, at a reasonable expense of accuracy compared to highly-resolved CFD simulations, while benefiting from lower runtimes compared to more traditional CFD approaches.

2 Methodology

The framework used in this study consists of a GPU enabled LBM fluid solver that is tightly coupled to the structural multi-body solver Dymore. The framework sends velocity data from the fluid solver, e.g. inflow and free stream flow conditions, every time step to the structural solver and the resulting rotor forces computed by blade element method are sent to the fluid solver and act as a source term in the fluid simulation. The coupling includes different modes that either include an actuator disc approach or an actuator line approach for the rotor modeling in the flow solver. The coupling modes and their formulation are described in the following section. Detailed information on the LBM formulation and the force term equations can be found in Refs. [17], [18], [19], [20].

2.1 Linear-harmonic coupling

The actuator disk approaches implemented for the coupling try to minimize the required exchanged data between the LBM simulation and Dymore simulation. In general one could compute and save the thrust distribution over a full rotation and interpolate the values on the fluid grid and then send the complete inflow distribution of the disk to the stuctural simulation and interpolate the velocities on the blade positions over whole the disk. Depending on the resolution of the fluid grid, the amount of blade elements of each blade, the number of blades and azimuth stepping in the structural dynamics simulation this could lead to a relatively large and for varying rotational speed changing amount of data that has to be exchanged in each time step and interpolated on both sides. Considering that the framework also focuses on computational efficiency a different approach was chosen.

In order to reduce the computational effort and minimize exchanged data the thrust and inflow distributions are represented with a Fourier series so only the respective coefficients have to be evaluated and exchanged. In a previous publication Bludau et a. (Ref. [9]) presented a linear-harmonic approach inspired by the Pitt-Peters three-state dynamic inflow model published in Ref. [21].

The thrust T is hereby represented as a function that assumes a constant pressure jump along the radial coordinate and only varies in a harmonic fashion in azimuth direction given as

$$T(r,\psi) = \sum_{i=0}^{N_\mathrm{h}} t_{i,c}\cos(\psi i) + t_{i,s}\sin(\psi i) \tag{1}$$

where $t_{i,c}$ is the cosine coefficient for the i-th harmonic computed as

$$t_{i,c} = \frac{2}{N_\Psi}\sum_{j=1}^{N_\mathrm{blade}}\sum_{k=1}^{N_\Psi} T_j(\Psi_k)\cos(i\Psi_k) \tag{2}$$

with T_j being the thrust in cell j. The computation of the sine coefficient $t_{i,s}$ is done respectively. The flow through the disk is represented with a linear approximation given as

$$u_i(r,\psi) = u_{i0} + u_{is}\frac{r}{R}\sin(\psi) + u_{ic}\frac{r}{R}\cos(\psi) \tag{3}$$

where u_i are the extracted velocities, ψ being the azimuth angle, and subscript $0,s,c$ indicating the mean, sine, and cosine coefficients, respectively. The coefficients are calculated by

$$u_{i0} = \frac{1}{N_\mathrm{cell}}\sum_{j=1}^{N_\mathrm{cell}} u_j \tag{4}$$

$$u_{is} = \frac{4}{N_\mathrm{cell}}\sum_{j=1}^{N_\mathrm{cell}} u_j\frac{r}{R}\sin(\psi) \tag{5}$$

$$u_{ic} = \frac{4}{N_\mathrm{cell}}\sum_{j=1}^{N_\mathrm{cell}} u_j\frac{r}{R}\cos(\psi) \tag{6}$$

with u_j being the velocity in each cell. It should be noted that thrust and velocity coefficients are computed for all directions, so not only the induced velocities perpendicular to the rotor disk are captured but also free stream conditions.

This approach has the advantage that only a small amount of data has to be exchanged, namely three coefficients for each velocity component and two times N_h coefficients for the thrust distribution. Furthermore, can thrust and velocity easily be evaluated at any position in the rotor disk without the need for more costly (higher order) interpolation. The coefficients are updated and exchanged each time step although an arbitrary exchange rate could be use. Nevertheless this set of functions acts as a strong filter for both radial changes in the thrust distribution and velocity disturbances less than one rotor radius. While this is considered sufficient for simulator flight mechanics accounting for disturbances in airflow when flying in challenging conditions such as ship landing operations, flight near buildings or having interaction of multiple rotors might be necessary.

2.2 Bessel-Fourier coupling

The fact that the linear-harmonic coupling acts as a strong filter on both the inflow and the thrust distribution lead to the extension of the linear-harmonic to the Bessel-Fourier model where the thrust distribution is approximated with a different set of base functions. This extension is inspired by the enhancement of the Pitt-Peters to the Peters-He inflow model presented in Ref. [22]. Contrary to the linear-harmonic model, the Bessel-Fourier model does not assume a constant pressure distribution in radial direction but rather uses Bessel functions to represent the radial change. The harmonic part in azimuth direction is unchanged to the rotors harmonic behaviour.

The thrust T with respect to radial location r and rotor azimuth location ψ, is represented by the sum over N_h harmonics in azimuth direction and N_r Bessel functions in radial direction.

$$T(r,\psi) = \sum_{j=0}^{N_{\mathrm{h},\psi}} \sum_{i=0}^{N_{\mathrm{r}}} t_{ij,c} J_1(j_{1,i} r)\cos(\psi j) + t_{ij,s} J_1(j_{1,i} r)\sin(\psi j) \tag{7}$$

where t_{ij} is the coefficient for the ij-th harmonic combination with the Bessel functions J_1 and $j_{1,i}$ being the i-th root.

$$t_{ij,c} = \sum_{k=0}^{N_{\mathrm{blade}}} \frac{2}{\pi J_2(j_{1,i})^2} \int_0^{2\pi} \int_0^R T_k(r,\psi) J_1(j_{1,i} r)\cos(\psi j) r \mathrm{d}r \mathrm{d}\psi \tag{8}$$

The integral in Eq. 8 is approximated as a discrete sum over the rotor disc comparable to Eq. 2. Because the Bessel functions require $J_1(R) = 0$ the representation of the velocity distribution with these functions is not feasible as an arbitrary velocity condition can prevail at the outer edge of the disc. Instead the velocities are interpolated to the current blade positions and sent to the structural dynamics solver for airload computation.

2.3 Actuator line coupling

Unlike the actuator disk coupling, the actuator line coupling pursues a more localized approach. The current aerodynamic forces of the blade are interpolated onto the fluid grid at the current blade position with a kernel function. The resulting flow velocities in the rotor disk are interpolated from the fluid grid onto the current blade element positions.

The thrust related force term T at any fluid cell is thereby given as

$$T(x,y,z) = -\sum_{i=0}^{N_{\mathrm{blades}}} \sum_{j=0}^{N_{\mathrm{be}}} t_{ij} \eta_{ij}(x,y,z) \tag{9}$$

with N_{blades} as the number of blades, N_{be} the number of blade elements on the blade, t_{ij} as the thrust at the respective blade element and η_{ij} as the kernel function detailed below.

There are different definitions present in literature for η. A commonly used approach in literature (Refs. [23], [24]) is

$$\eta_{ij} = \frac{1}{\varepsilon^3 \pi^{3/2}} \exp\left[-(|r_D|/\varepsilon)^2\right] \tag{10}$$

with r_D being the shortest distance between the blade element position and the fluid cell position and ε being the kernel width. This leads to a spherical appearance of the force distribution with respect to the blade element. Furthermore the spheres of neighboring blade elements do overlap so that a single fluid cell can get force contributions from multiple blade elements. To counter this problem Schmitz et al. (Ref. [25]) proposed an "actuator curve embedded" approach, where each cell is only influenced by a single blade element. This is achieved by computing the shortest perpendicular distance p_N between the actuator line, e.g. blade direction, and a respective fluid cell. Then only the force term of the blade element closest to the intersection between distance vector and blade radial vector is applied on the fluid cell. The kernel is then given by

$$\eta_{ij} = \frac{1}{\varepsilon^2 \pi \Delta_b} \exp\left[-(p_N/\varepsilon)^2\right] \tag{11}$$

with Δ_b as the blade element width. Both approaches for the kernel are applied in this study and compared with respect to overall results and stability.

One significant difference arises from the locality of the forcing term compared to the actuator disc models. The distribution kernel η introduces a vortex with a vortex core size depending on the kernel size as discussed in Ref. [26] in addition to the tip vortex that forms at the blade tip and have an additional effect on the velocity sampling and the resulting aerodynamic force computation. This makes inflow sampling not as straightforward as for the AD approaches and is discussed in the next section.

2.4 Inflow sampling and Tip Correction

The inflow sampling and tip correction poses an additional challenge for the ACL appraoch. The kernel width for most simulations is larger than the optimal kernel width due to coarse grids and leads to incorrect blade loadings and tip losses in the region of the blade tip. Various authors (Refs. [27], [28], [26], [6]) have presented suggestions on how to account for these influences.

The approach used in this study is derived from the filtered lifting line theory presented by Martinez-Tossas and Menevau (Ref. [26]) where the sampled inflow velocity is adjusted, e.g. the vertical flow component, to correctly account for tip losses and the effect of the Gaussian kernel. In short the velocity is sampled at the current quarter chord line position of the blade and the algorithm iteratively adjusts the inflow component depending on the variation of bound vorticity along the blade. A detailed derivation can be found in the respective publication and is not elaborated here. It should be noted that this approach was developed for a non rotating wing. A similar proposal by Dağ et al. (Ref. [27]) included a correction for rotating blades where the rotor wake shape needs to be computed as well. As this includes computational overhead the simplified correction was used.

A second approach is an integrated velocity sampling used by Refs. [29], [6], where the velocities are not extracted at the current blade position in the fluid domain but rather as a circular integrated average. The circular region has a given radius and its surface is perpendicular to the blade radial direction. This approach averages out the effect of the kernel induced vortex.

With the second approach no special care was taken for the tip where the tip vortex develops. In combination with the 2D airfoil table lookup used this lead to an overprediction of forces at the blade tip. The same is true for the AD models, where a steady vortex is present at the boundary of the rotor disk due to the pressure jump. A simple feature already present in Dymore was used, where a tip loss factor C_{TL} forces the lift to zero at the blade tip. This factor is also used for all computations with the internal Peters-He inflow model which will serve as a reference for all results.

$$C_{\mathrm{TL}} = \tanh\left(\frac{1-r}{1-l}\right) \tag{12}$$

$$C_{\mathrm{TL},\%} = 1 - \int_{\mathrm{r}=0}^{1} \tanh\left(\frac{1-r}{1-l}\right) \mathrm{d}r \tag{13}$$

The factor l varies in theory from 0-1 and is in reality often between 0.93 and 0.97. In theory the ACL velocity sampling with the tip correction should not need this additional factor, but results showed that the tip correction alone let to instabilites at the blade tip when $C_{\mathrm{TL},\%} = 0\%$ was used.

In the following study all inflow models use C_{TL} whereby the parameter l is varied. The actuator line model will additionally use the tip correction or the integral velocity sampling with an integration radius of one chord length.

3 Simulation setup and rotor models

This study investigates two different rotors, one being an experimental teetering rotor and the other one the UH60A rotor used extensively in literature for validation purposes. For both rotors the simulation setup is divided in a hover and a wind tunnel setup depending on the experimental conditions.

3.1 LBM simulation setup

The hover setup consist of a rectangular domain with an edge length of six rotor radii in plane the rotor plane and twelve rotor radii perpendicular to the rotor plane. The rotor was placed in the center of the domain. All boundaries were defined as free outflow boundaries modeled as an impedance boundary formulation (Ref. [30]). The rotor hub was not accurately modeled but was represented with a solid sphere to prohibit upwards flow in the rotor center.

The wind tunnel setup consists of a rectangular domain that has a length of 24 rotor radii and a width and height of ten rotor radii. The inlet is a velocity boundary were the free stream velocity was prescribed. The outlet is the aforementioned impedance boundary. The walls of the wind tunnel are modeled with curved wall boundary model (Ref. [31]) to account for the effect of non aligned walls with respect to the Cartesian grid. The inclination of the top and bottom boundary depends on the shaft angle of attack of the rotor. This was necessary as the rotor plane should be aligned with the Cartesian grid and therefore the rotor itself cannot be tilted with respect to the fluid grid.

3.2 Dymore rotor models

The experimental rotor used for the first part of the study is a teetering rotor with two rectangular blades without any twist or taper and a radius of 2.32 meters. The airfoil was a NACA0012 and the blades were considered stiff. Further details can be found in the respective report (Ref. [15]). The rotor was modeled in Dymore and the aerodynamics forces are computed via blade element theory and 2D airfoil tables.

The UH60 rotor used in the second part of the study was largely based of of the UH60 Dymore model presented in a previous paper by Rex et al. (Ref. [32]), with some minor adjustments to sensor output and the aerodynamic force computation. Further information about the rotor model can be found in the respective publication and is not detailed in this paper.

4 Experimental Rotor Results and Discussion

The focus for the experimental rotor was the variation of the simulation parameters for the tip correction and the tip loss parameter l and the used resolution in the flow simulation and derive parameter estimates. The findings are applied for the UH60A rotor in the second part of this study.

4.1 Hover results

Figure 1 shows the power prediction for all the different models in hover conditions. The increasing blade pitch input corresponds Θ_0 to an increasing C_T. The data for the Dymore internal Peters-He inflow model shows a constant overprediction of the power for all trimmed thrust conditions. The impact of the tip loss factor can be clearly seen, with a higher tip loss leading to higher power predictions. The best match is for the smallest tip loss of about four percent. An even lower tip loss led to instabilities in the inflow computation due to constraints of the formulation of the Peters-He model at the blade tip. The results for the linear-harmonic coupling show an declining power prediction with increasing Θ_0. This leads to overpredictions in the low pitch case but turns to underpredictions of up to -20% for the highest tip loss of 11% and the highest resolution of 80 cells per blade radius. The results show that the change in power prediction between 64 and 80 cells per radius is negligible. Additionally, the results for 16 cells per radius are clearly distinct from the others and the resolution be seen as too low. The influence of the tip loss is comparable to the Peters-He data. The Bessel-Fourier coupling shows overprediction at lower thrust and underprediction for higher thrusts. It is noticeable that the different resolutions are quite distinct except for the highest thrust condition where the distinction between the power prediction is primarily from the variation of the tip loss factor.

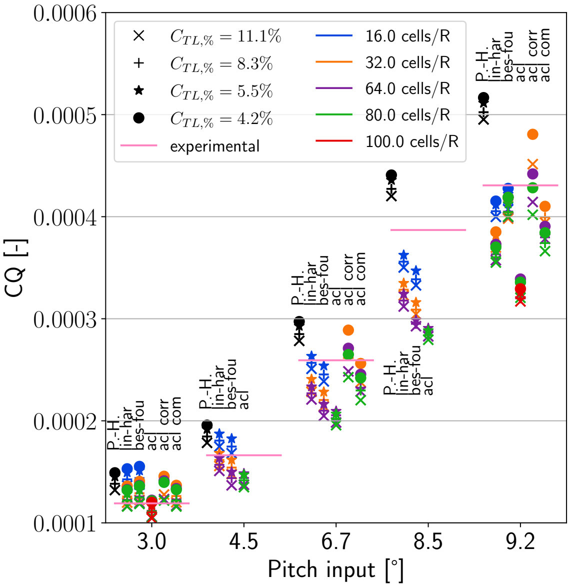

Fig. 1: Power predictions compared to experimental measurements for the Peters-He (P.-H.), linear-harmonic (lin-harm), Bessel-Fourier (bes-fou), actuator line model with kernel as Eq. 11 (acl), common kernel Eq. 10 (acl comm) and corrected kernel (acl corr) inflow models.

The result for the actuator line kernel according to Eq. 11 show a trend for the power prediction that is similar to the other models, but already starting with an underprediction for low θ_0 and increasingly underestimating power for higher pitch values. For inputs starting from $\theta_0 = 6.7°$ error is significant with up to -20%. Nevertheless, results are distinguished by tip loss rather than resolution. The results for the actuator line with the common kernel function according to Eq. 10 show an overprediction in power for low pitch but unterpredict power for the higher pitch cases again. The distinct differences in the tip loss factor can be clearly seen as well as an influence of the resolution. The results for the common kernel with the tipcorrection do not show a trend as the other models but rater stay in the same error bandwidth independent of the given blade input. Nevertheless the tip loss still has a significant effect on the results.

Evaluation of the computed inflow shows that increasing resolution for the Bessel-Fourier model leads to an instability in the inner blade section (see Figure 2). This had the effect that a grid convergence could not be achieved for the Bessel-Fourier model. The severity of the instability decreases with increasing C_T. Further investigation showed that this instability results from a combination of multiple effects. First the Bessel functions approximate the thrust distribution from the rotor center to the blade tip. This leads to a sudden jump of pressure when the blade switches from aerodynamic ineffective region to the aerodynamic effective region plus a flat zero region for the part of the disc further inside. This leads to the occurence of Gibb's phenomena in the inner section of the blade due to the approximation. On the one hand this introduces oscillations in the approximated pressure distribution that are reflected in the resulting inflow velocities. On the other hand a small phase error is introduced, which leads to peaks and sinks in the inflow that are not in line with the lift peaks and sinks of the actual spanwise distribution. This leads to resonance between inflow and lift. For low pitch angles the overall inflow velocity is low in the inner blade sections as well as the rotational speed of the blade in the inner section. The combination of these two conditions leads to a high sensitivity of the angle of attack, e.g. lift, with respect to small errors in the inflow. This effect diminishes with increasing pitch input. Lower resolutions in the flow simulation act as a filter on the lift distribution applied in the flow simulation and is therefore more stable compared to higher resolutions.

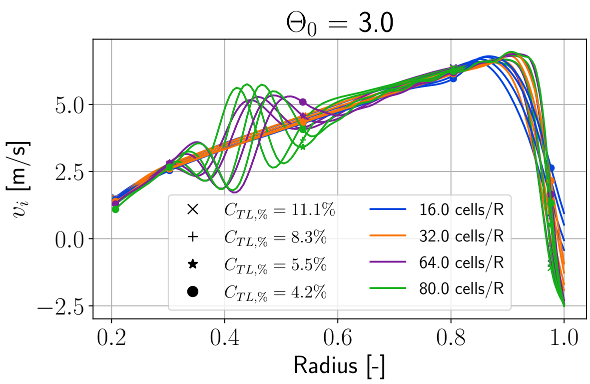

Fig. 2: Radial inflow distribution of the Bessel-Fourier model with clearly visible instabilities that increase with resolution.

Figure 3 shows the radial lift distribution for the actuator line with the kernel according to Eq. 11. The instabilities in the data are clearly visible for this kernel that spread out with increasing resolution. Further investigations not shown in this study showed similar behaviour even for simple wing cases with a steady free stream velocity and fixed angle of attack. The reason for this behaviour could not be determined and led to the usage of the common kernel for the actuator line method. Neither the common kernel without or with the tip correction showed instabilities for any chosen resolution or given pitch input (see Appendix A).

The effect of the tip loss factor is clearly visible for all models and are even visible in Figures 3, 2 despite the occurring instabilities. A lower tip loss pushes the inflow peak more outboard than a higher one as is to be expected since the slope is significantly steeper for C_{TL}. The same is true for the lift peak. It can also be clearly seen that the inflow drop is very steep for the LBM coupled inflow (see Figure 2 compared to the Peters-He inflow (see Figure 4. Therefore a high tip loss is required for the LBM computed inflow to match experimental data in blade tip region, whereas the Peters-He model requires a tip loss (see Figure 5) that is in the expected range of three to five percent.

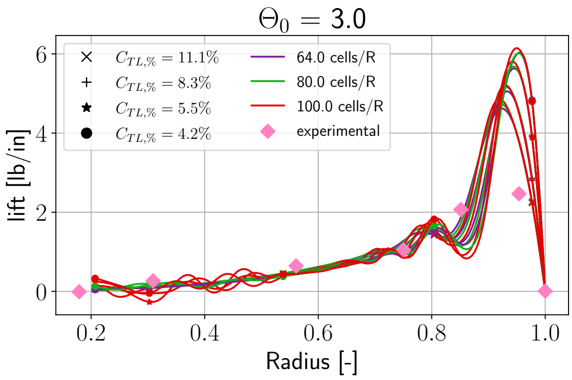

Fig. 3: Radial lift distribution of the ACL model with $\Theta_0 = 3.0°$ with instabilities for higher resolutions.

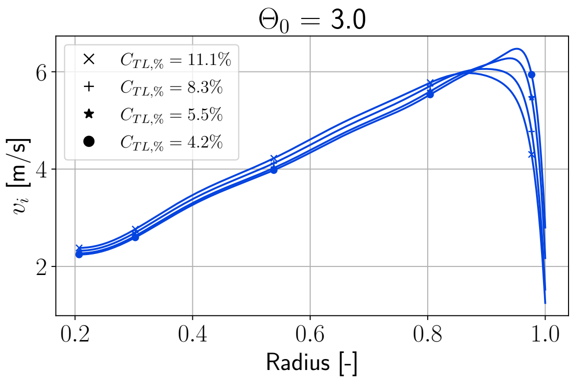

Fig. 4: Radial inflow distribution of the Peters-He model with $\Theta_0 = 3.0°$

Overall, the results for the hover cases show that the LBM coupling tends to underpredict the rotor power while the Peters-He overpredicts the power. The actuator line coupling with the non common kernel and the Besser-Fourier coupling show instability issues for higher resolutions.

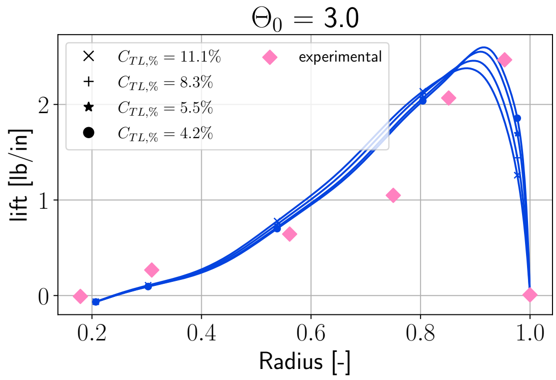

Fig. 5: Radial lift distribution of the Peters-He model with $\Theta_0 = 3.0°$

4.2 Wind tunnel results

In the following the results for the windtunnel experiments are shown for three different advance ratios $\mu = [0.08, 0.20, 0.29$. The shaft was tilted according to measurements in Ref. [16]. The rotor was trimmed to lift and drag and to zero side forces.

The trends for the power predictions are similar for all coupling modes as well as the Peters-He inflow model. The error increases with increasing advance ratio. For $\mu = 0.08$ the LBM inflow models underpredict the power up to 25% percent for the actuator line model with the common kernel, this is in line with the results for the hover cases. The Peters-He model overpredicts the power between 15% to 20%. For all higher advance ratios all inflow models overpredict the power consumption by up to 60%. The correction for the actuator line model leads to higher power predictions compared to the uncorrected one. The best predictions are shown by the Bessel-Fourier model with a maximum error at $\mu = 0.29$ of 13%. For all inflow models the effect of the resolution is negligible compared to the tip loss factor which is the major influence factor.

The comparison of experimental measurements at five radial locations over a full rotor rotation with computational results allow a detailed look in the performance of the different inflow models. The results for the Peters-He model (see Figure 7) show that the $\mu = 0.08$ case does not reflect the peak to peak values nor the trend. This improves with increasing advance ratio where the trends match better. The peak values are overpredicted for the outer radial stations especially around $\psi = 180°$. The tip loss factor effect is low for all radial stations except at 95% radius which is consistent with the results in hover. For the linear-harmonic model the limitations of the formulation are clearly visible in the reduced capability to represent the trends over one rotation (see Figures 22,23). This improves for higher advance ratios. The effect of resolution or tip loss is low except for the most outboard station. The Bessel-Fourier coupling results meet the trends well even for $\mu = 0.08$ (see Figures 24, 25). The results for the actuator line models show good agreement with the trends and peak to peak values, except

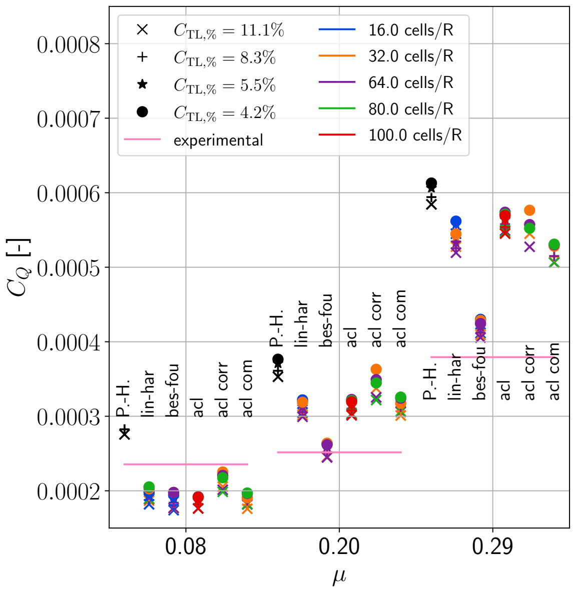

Fig. 6: Power predictions compared to experimental measurements for the Peters-He (P.-H.), linear-harmonic (lin-harm), Bessel-Fourier (bes-fou), actuator line model with kernel as Eq. 11 (acl), common kernel Eq. 10 (acl comm) and corrected kernel (acl corr) inflow models.

for the most outboard radial station where the overall lift is overestimated for the full rotation (see Figures 26, 27, 29, 29). One major difference for the corrected version are the lower lift estimates for the outboard radial station. For a tip loss of 11% the loads are even underestimated (see Figures 30,31).

All models overpredict the loads between 120° and 220° azimuth with increasing advance ratio and do not match the peaks well for the 95% radial station. The first issue might come from the limitations of 2D airfoil theory where cross flow conditions such as the front of the rotor experiences cannot be adequately modeled. The prediction of lift close to the blade tip also suffers from the fact that in reality it is a heavily three-dimensional flow that is not adequately modeled with 2D airfoil tables. Furthermore, the tip correction employed might not be sufficient to predict accurate loads in this section of the blade.

When comparing the predicted longitudinal flap with the measurements, all models predict a maximum of 0.5° higher flap angle for $\mu = 0.08$. The Peters-He and the linear-harmonic models slightly overpredict by 0.1 degree. For higher μ, all models predict decreasing flap angles, with a maximum error of 0.5 degree at 0.29μ. Actuator line models using the common kernel exhibit a lower error, up to 0.3 degree. All models predict flapping angles within a 0.5 degree bandwidth, and neither the tip loss nor the resolution of the fluid simulation significantly affects the flapping angle. The validity of the measurements for the lateral flap was uncertain, as the trim condition of zero side force is expected to produce zero lateral flap, consistent with the simulations. However, the measurements indicated a lateral flap of approximately 2 degrees for all advance ratios.

4.3 Preliminary findings

The results provide valuable insights into the LBM calculated inflow in comparison to experimental data and the commonly used Peters-He inflow model. All models encounter issues in predicting power for the experimental rotor. The Peters-He model overestimates power usage for all test conditions, with a significant impact of the tip loss factor on power prediction. The LBM inflow computation underestimates power for hovering and low advance ratios and overestimates power with increasing advance ratio. For hover simulations, both resolution and tip loss factor impact power prediction, in contrast to wind tunnel results where resolution seems to have a negligible impact. The results indicate that the radial loads can be predicted using the LBM computed inflow except for the blade tip area. Nevertheless, this is limited for the linear-harmonic model because the underlying base functions that describe the coupled quantities are restricted.

It should be kept in mind that the rotor blades are rectangular without any twist or taper and a low aspect ratio. These conditions lead to a strong curvature in the outer blade section and make it harder for any function based representation to capture the trend. Furthermore a significant part of the total lift and drag are produced in a region where a blade element approach might not lead to best results. The investigation of the UH60A rotor results show if these issues persist with rotor design used in operations.

Another important finding is the stability issue of the actuator line with the kernel according to Eq. 11 in combination with higher resolutions. The reason for this behaviour could not be determined, but can be resolved by using the common kernel. The Bessel-Fourier model experienced stability issues in the inner section of the blade due to approximation errors for low C_T during hover conditions. No such behavior was observed for the wind tunnel simulations.

The drop of the inflow at the blade tip that is steeper than for the Peters-He model contributes to a higher angle of attack and thereby strongly increased loads in the tip region. This drop results from the forming of a vortex at the blade tip due to the pressure jump that introduces an upwash. This upwash increases the angle of attack and therefore generated lift with the 2D airfoil and blade elements. A higher tip loss factor is needed to reduce this effect of the vortex on the airloads.

In summary, all models produced plausible results, but none of them provided satisfactory power predictions. Nevertheless, the study's results indicate that a higher tip loss factor and a resolution of at least 64 cells per rotor radius result in optimal performance for all LBM models. These findings can be applied to the use of LBM inflow modeling for the UH60A rotor. It is recommended to select a tip loss value of approximately 9% for the LBM inflow.

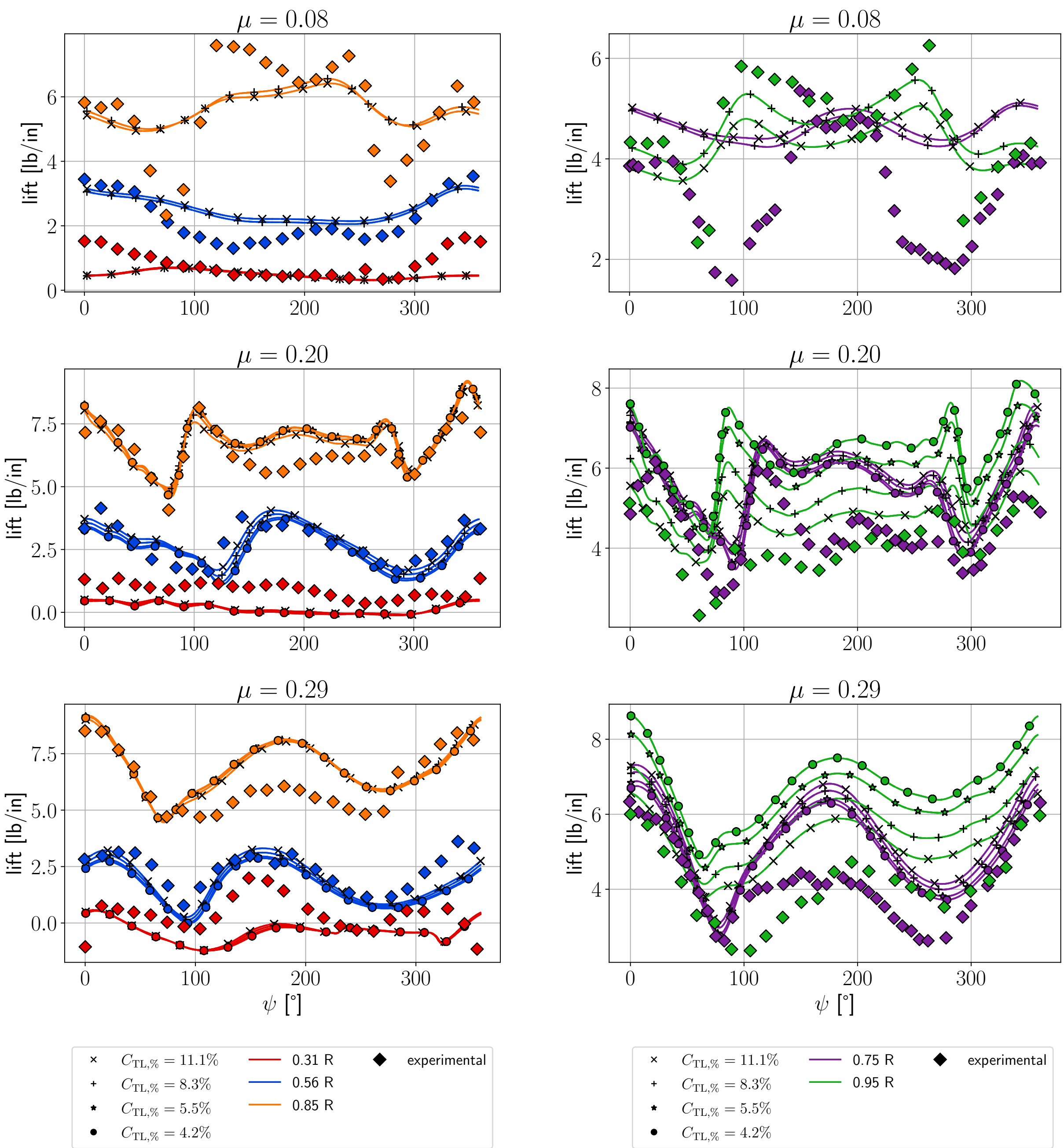

Fig. 7: Azimuth lift variation at five radial stations for different resolutions and tip loss for the Peters-He inflow model

5 UH60A Results and Discussion

With the experimental rotor results, the simulation settings were established by fixing the resolution at 64 cells per radius and setting the tip loss factor to nine percent in all simulations. The Peters-He tip loss was set to four percent. The experimental data is from wind tunnel measurements taken from Ref. [33] and the airloads program flight test program taken from Ref. [34]. The wind tunnel experiments were trimmed to zero flap and the measured thrust. The flight test results were trimmed to thrust and the measured hub moments.

Figure 9 displays the $\frac{C_P}{\sigma}$ predictions and the error in the predictions compared to experimental and flight test measurements. The Peters-He model's results agree well with flight test data, with an error of no more than -15% for the lowest advance ratio, and the rest of the results falling within a range of +/-6%. The error increases as the advance ratio increases when comparing with the wind tunnel results, but it remains within -10% to +20% at $\mu = 0.19$ and $\frac{C_T}{\sigma} = 0.09$.

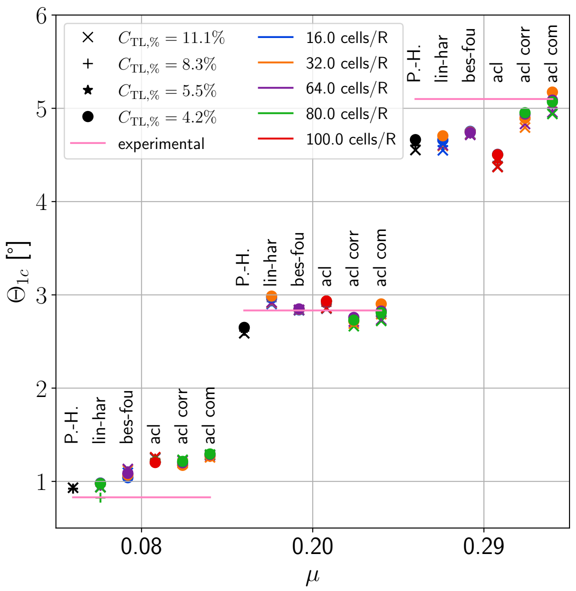

Fig. 8: Longitudinal pitch input predictions compared to experimental measurements for the Peters-He (P.-H.), linear-harmonic (lin-harm), Bessel-Fourier (bes-fou), actuator line model with kernel as Eq. 11 (acl), common kernel Eq. 10 (acl comm) and corrected kernel (acl corr) inflow models.

The flight test data agrees well at this speed, indicating that there may be wind tunnel effects that were not modeled. The actuator line results using the common kernel agree well with the test data, but they underestimate performance until $\mu = 0.19$ and overestimate it for high advance ratios. The wind tunnel simulations exhibit an error exceeding 20% for the low μ cases, but the error diminishes with an increasing advance ratio. One plausible explanation is that the simulated domain is too small, which does not alleviate the wall effects in the LBM simulation. Similarly, the Bessel-Fourier coupling displays similar trends, but accurately predicts the flight test performance within a range of 10%. The linear-harmonic coupling model underestimates the power for all circumstances. This might be due to the inflow and pressure representation that approximate the distribution as to optimistic.

The longitudinal flap results of the Peters-He model depict the trend accurately up to $\mu = 0.23$ with an offset of approximately 0.5 degrees. At higher advance ratios, the predicted flap angles are lower than the measurements, but the overall trend is still visible. The actuator line model and the Bessel-Fourier model exhibit similar trends to the Peters-He results. The trend for the lateral flap motion is not well predicted between $\mu = 0.15 - 0.27$. However, at this point, no apparent reason has been found for this behavior. The linear-harmonic model does not show a significant offset for the lateral flap motion and accurately predicts the trend for $\mu = 0.15 - 0.27$. However, for higher advance ratios, the model overpredicts the lateral flap angle.

The feathering input from the simulation trim (Figure 12)

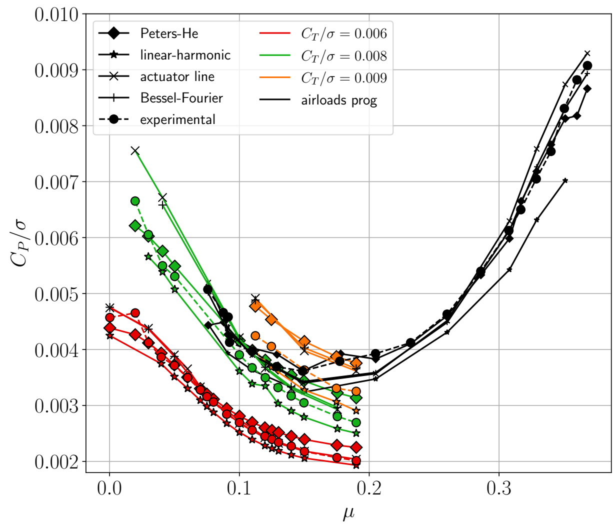

Fig. 9: Rotor power results, experimental results from the airloads program are taken from Ref. [33], wind tunnel measurements from Ref. [34].

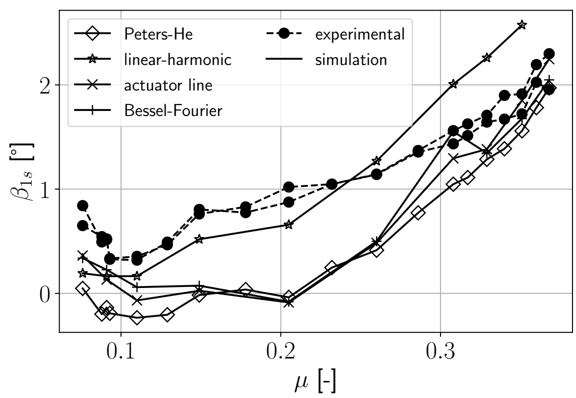

Fig. 10: Lateral flap, experimental results from the airloads program are taken from Ref. [34].

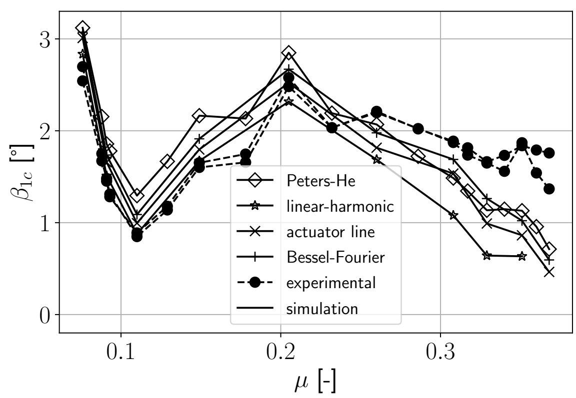

Fig. 11: Longitudinal flap, experimental results from the airloads program are taken from Ref. [34].

and the measurements exhibit good agreement for all models regarding the collective and longitudinal input. However, the linear-harmonic model inadequately represents the trend for the lateral input and has an obvious offset of around four degrees. Additionally, the collective trend does not fully capture the slope at higher μ. The Peters-He model inadequately represents the trend for low values of μ, but is otherwise on par with the Bessel-Fourier and actuator line models. All models capture the trend for longitudinal input between $\mu = 0.04..0.15$, but overestimate input for the highest advance ratios.

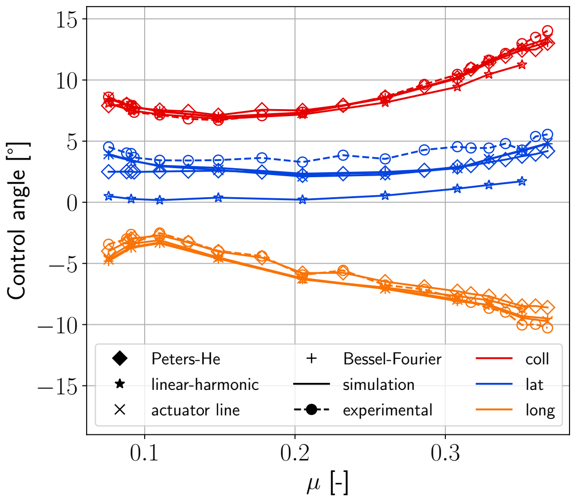

Fig. 12: Feathering input at the blade root. Experimental results from the airloads program are taken from Ref. [34].

The cause of better performance for the lateral blade flap with less accurate lateral input prediction remains unclear. Given the complex interaction between controls, inflow, and blade motion, this study refrains from speculating on the underlying reasons for this phenomenon as further investigations are needed.

In general, the findings are satisfactory. In particular, the considerably improved power prediction in comparison to the experimental rotor for both zero flap wind tunnel trim and level flight trim, indicates the potential that the experimental rotor's design impedes power predictions for all models.

6 Summary & Conclusion

In summary, the Lattice-Boltzmann Method, coupled with Dymore, computed inflow resulting in comparable rotor performance to that observed through the Peters-He inflow for both the experimental and UH60A rotors.

Analysis of the experimental rotor in hover showed that power was underestimated for the LBM cases and overestimated for the Peters-He inflow. The treatment of tip loss greatly influenced the power prediction and radial lift distribution for all models. The resolution of the flow simulation was an influence factor to some extent. The experimental rotor's results under wind tunnel conditions showed an increasing power (over)prediction for all models except the Bessel-Fourier model, which predicted power within a constant bandwidth. The actuator line and Bessel-Fourier coupling showed a satisfactory agreement for the azimuth load distribution. The linear harmonic results were limited by their limited ability to represent the radial flow distribution. As anticipated, the treatment for tip loss exhibited a significant effect on the outer sections of the blade, while the impact of resolution was limited on the outcomes.

The power predictions for the UH60A rotor were compared with the power measurements obtained during the wind tunnel tests and flight tests. All models predicted the performance well for the flight tests. However, for the wind tunnel results power prediction were overestimated with increasing C_T/σ. Control predictions were in close agreement with the measurements except for the linear harmonic, which consistently underestimated the lateral input by about four degrees. The flap results matched longitudinal flapping trends well, but there were shortcomings in predicting lateral flap behavior for the actuator line and Bessel-Fourier coupling models.

A range of conclusions can be drawn from the results of this study.

- It is evident that the treatment of the tip significantly affects the lift in the outboard section of the blade as well as the power predictions. While a simple tip loss factor is adequate for achieving good results with the UH60A rotor, it is not sufficient for the non-optimized shape of the experimental rotor. The additional tip correction approach yielded good performance for hover results, but not for a rotor in edgewise flow conditions. As a consequence it is necessary to examine the tip loss treatment in detail to enhance power prediction for all flight conditions and rotor shapes.

- The linear-harmonic model, being the simplest model in terms of degrees of freedom, is still capable of obtaining comparable integrated results such as power and control as well as flap motion.

- The Bessel-Fourier model serves as an enhancement of the linear-harmonic coupling and yields superior overall results, but experiences stability issues in hover for low C_T, which restricts its universal applicability.

- The model utilizing actuator line coupling for the rotor yields better results than the actuator disc methods, but only for the commonly used spherical force distribution kernel. Using the actuator curve embedded approach led to instabilities.

- A resolution of 64 cells per radius is adequate for all coupling models and potentially less if computational speed outweighs improved accuracy.

The presented study demonstrates the effectiveness of Lattice-Boltzmann in a mid-fidelity CFD/CSD coupling without the need for modeling blade geometry in the flow solver.

This approach allows for low resolutions and reasonable computational time. Consequently, this method enables the study of mission scenarios in complex flow environments, such as landing procedures in wake conditions behind structures or moving objects, for varying mission parameters within a reasonable time frame. As a next step, it is necessary to validate the coupling against flight test data to enhance confidence in the simulation of dynamic rotorcraft response to conduct actual mission simulations.

7 Acknowledgements

This work is part of the project "Lattice-Boltzmann unterstuetzter Reglerentwurf" (reference HAM-2109-0045) funded under the "Bayerisches Luftfahrtforschungsprogramm - Holistische Air Mobility Initiative Bayern" program.

Sponsored by

Bavarian Ministry of Economic Affairs, Regional Development and Energy

8 References

[1]Xin, H., Goss, J., and Parkes, C., "Development of a three-state rotor interference model and application to coaxial rotor inflow modeling," *American Helicopter Society Aeromechanics Specialists Conference*, 2014.

[2]Sørensen, J. N. and Myken, A., "Unsteady actuator disc model for horizontal axis wind turbines," *Journal of Wind Engineering and Industrial Aerodynamics*, Vol. 39, No. 1, 1992, pp. 139–149.

[3]Le Chuiton, F., "Actuator disc modelling for helicopter rotors," *Aerospace Science and Technology*, Vol. 8, No. 4, 2004, pp. 285–297.

[4]Barakos, G., Fitzgibbon, T., Kusyumov, A., KUSYUMOV, S., and Mikhailov, S., "CFD simulation of helicopter rotor flow based on unsteady actuator disk model," *Chinese Journal of Aeronautics*, Vol. 33, No. 9, 2020, pp. 2313–2328.

[5]Ahmad, J. U., "Application of Rotor Disk Model in the OVERFLOW CFD Code," Tech. Rep. NASA/TM—20220005496, NASA, 2022.

[6]Chiew, J., Aftosmis, M., and Manies, K. L., "Medium-Fidelity CFD Modeling of Multicopter Wakes for Airborne Sensor Measurements," *78th Annual Vertical Flight Society Forum and Technology Display*, Ft. Worth, Texas, USA, May 10–12, 2022.

[7]Jha, P. K., Churchfield, M. J., Moriarty, P. J., and Schmitz, S., "Guidelines for Volume Force Distributions Within Actuator Line Modeling of Wind Turbines on Large-Eddy Simulation-Type Grids," *Journal of Solar Energy Engineering*, Vol. 136, No. 3, 01 2014, pp. 031003.

[8]Friedmann, L., Ohmer, P., and Hajek, M., "Real-time simulation of rotorcraft downwash in proximity of complex obstacles using grid-based approaches," *Annual Forum Proceedings-AHS International*, 2014.

[9]Bludau, J., Rauleder, J., Friedmann, L., and Hajek, M., "Real-Time Simulation of Dynamic Inflow Using Rotorcraft Flight Dynamics Coupled With a Lattice-Boltzmann Based Fluid Simulation," *55th AIAA Aerospace Sciences Meeting, AIAA SciTech*, Grapewine, TX, 2017.

[10]Bludau, J., Rauleder, J., and Hajek, M., "Validation of a Dynamic Inflow Model Based on a Flight Dynamics Model and a Lattice-Boltzmann Fluid Solver Using Flight Test Data," *43rd European Rotorcraft Forum*, Milan, Italy, 2017.

[11]Horvat, B., Hajek, M., and Rauleder, J., "Analysing Rotorcraft Vortex Encounter Methods with a Lattice-Boltzmann Method Based GPU Framework," *AIAA Science and Technology Forum*, Orlando, FL, 2020.

[12]Horvat, B., Hajek, M., and Rauleder, J., *Computational Flight Path Analysis of a Helicopter in an Offshore Wind Farm using a Lattice-Boltzmann Method*, 2021.

[13]Bludau, J., Rauleder, J., and Hajek, M., "Solving the Ship-Rotorcraft Dynamic Interface Problem Using Lattice-Boltzmann Aerodynamics Two-Way Coupled with Blade Element Based Flight Dynamics," *VFS International 77th Annual Forum and Technology Display*, Virtual, 2021.

[14]Bauchau, O. A., Bottasso, C. L., and Nikishkov, Y. G., "Modeling rotorcraft dynamics with finite element multibody procedures," *Mathematical and Computer Modelling*, Vol. 33, No. 10-11, 2001, pp. 1113–1137.

[15]Rabbott Jr, J. P., "Static-thrust measurements of the aerodynamic loading on a helicopter rotor blade," Tech. rep., National Aeronautics and Space Administration Washington DC, 1956.

[16]Rabbott Jr, R. P. and Churchill, G. B., "Experimental investigation of the aerodynamic loading on a helicopter rotor blade in forward flight," Tech. rep., 1956.

[17]He, X. and Luo, L.-S., "Theory of the lattice Boltzmann method: From the Boltzmann equation to the lattice Boltzmann equation," *Physical Review E*, Vol. 56, No. 6, 1997, pp. 6811.

[18]Gross, E. P. and Krook, M., "Model for Collision Processes in Gases: Small-Amplitude Oscillations of Charged Two-Component Systems," *Phys. Rev.*, Vol. 102, May 1956, pp. 593–604.

[19]Wei, X., Li, W., Mueller, K., and Kaufman, A. E., "The Lattice-Boltzmann method for simulating gaseous phenomena," *IEEE Transactions on Visualization and Computer Graphics*, Vol. 10, No. 2, 2004, pp. 164–176.

[20]Guo, Z., Zheng, C., and Shi, B., "Discrete lattice effects on the forcing term in the lattice Boltzmann method," *Physical review E*, Vol. 65, No. 4, 2002, pp. 046308.

[21]Pitt, D. M. and Peters, D. A., "Theoretical prediction of dynamic-inflow derivatives," *6th European Rotorcraft Forum*, Bristol, England, 1980.

[22]Peters, D. A. and He, C. J., "Finite state induced flow models. II-Three-dimensional rotor disk," *Journal of Aircraft*, Vol. 32, No. 2, 1995, pp. 323–333.

[23]Sørensen, J. N. and Shen, W. Z., "Numerical Modeling of Wind Turbine Wakes ," *Journal of Fluids Engineering*, Vol. 124, No. 2, 05 2002, pp. 393–399.

[24]Churchfield, M. J., Lee, S., Michalakes, J., and Moriarty, P. J., "A numerical study of the effects of atmospheric and wake turbulence on wind turbine dynamics," *Journal of Turbulence*, Vol. 13, 2012, pp. N14.

[25]Jha, P. K. and Schmitz, S., "Actuator curve embedding – an advanced actuator line model," *Journal of Fluid Mechanics*, Vol. 834, 2018, pp. R2.

[26]Martínez-Tossas, L. A. and Meneveau, C., "Filtered lifting line theory and application to the actuator line model," *Journal of Fluid Mechanics*, Vol. 863, 2019, pp. 269–292.

[27]Dağ, K. O. and Sørensen, J. N., "A new tip correction for actuator line computations," *Wind Energy*, Vol. 23, No. 2, 2020, pp. 148–160.

[28]Melani, P., Balduzzi, F., and Bianchini, A., "Simulating tip effects in vertical-axis wind turbines with the actuator line method," *Journal of Physics: Conference Series*, Vol. 2265, IOP Publishing, 2022, p. 032028.

[29]Jost, E., Klein, L., Leipprand, H., Lutz, T., and Krämer, E., "Extracting the angle of attack on rotor blades from CFD simulations," *Wind Energy*, Vol. 21, No. 10, 2018, pp. 807–822.

[30]Schlaffer, M. B., *Non-reflecting boundary conditions for the lattice Boltzmann method*, Ph.D. thesis, Technische Universität München, 2013.

[31]Mei, R., Luo, L.-S., and Shyy, W., "An Accurate Curved Boundary Treatment in the Lattice Boltzmann Method," *Journal of Computational Physics*, Vol. 155, No. 2, 1999, pp. 307–330.

[32]Rex, W., Pflumm, T., and Hajek, M., "UH-60A Rotor and Coupled Rotor-Fuselage Simulation Framework Validation and Analysis," *45th European Rotorcraft Forum*, Warsaw, Poland, 2019.

[33]Shinoda, P. M., Yeo, H., and Norman, T. R., "Rotor performance of a UH-60 rotor system in the NASA Ames 80-by 120-Foot Wind Tunnel," *Journal of the American Helicopter Society*, Vol. 49, No. 4, 2004, pp. 401–413.

[34]Yeo, H., Bousman, W. G., and Johnson, W., "Performance analysis of a utility helicopter with standard and advanced rotors," *Journal of the American Helicopter Society*, Vol. 49, No. 3, 2004, pp. 250–270.

A Appendix

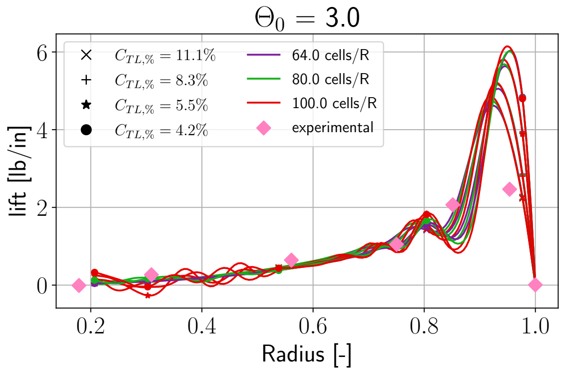

Fig. 13: Actuator line model

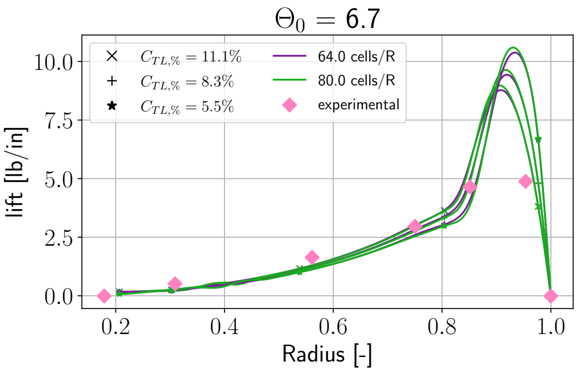

Fig. 14: Actuator line model

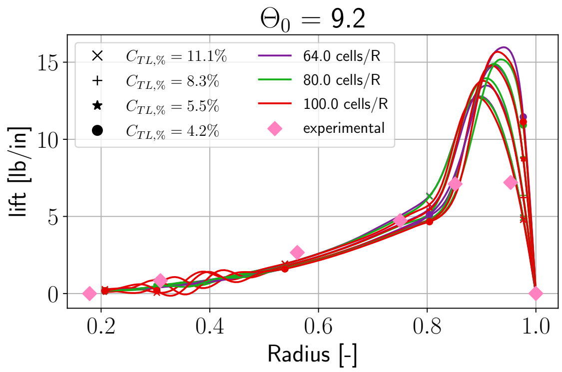

Fig. 15: Actuator line model

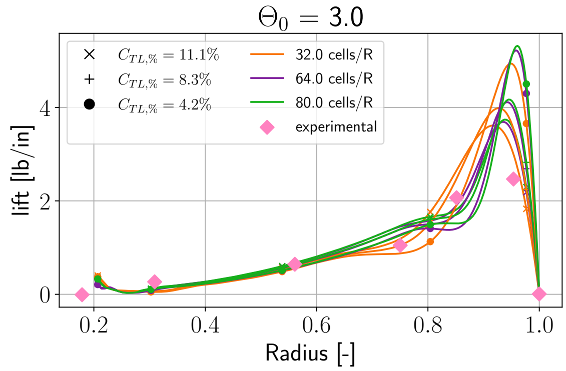

Fig. 16: Actuator line model with common kernel

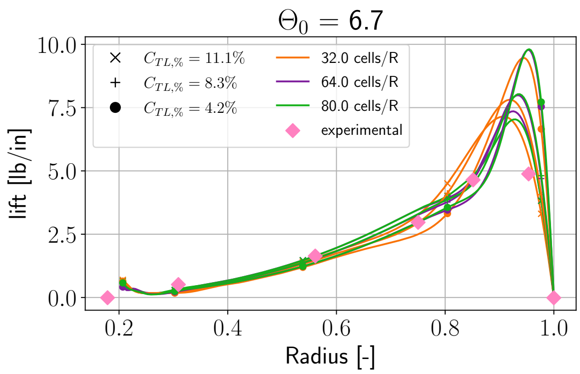

Fig. 17: Actuator line model with common kernel

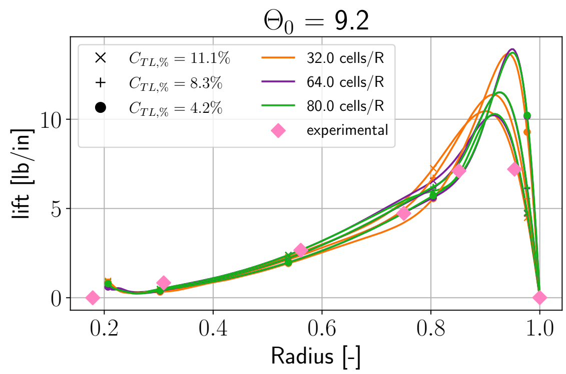

Fig. 18: Actuator line model with common kernel

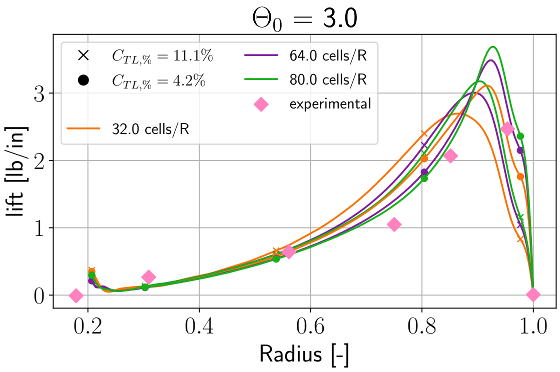

Fig. 19: Actuator line model with tip correction

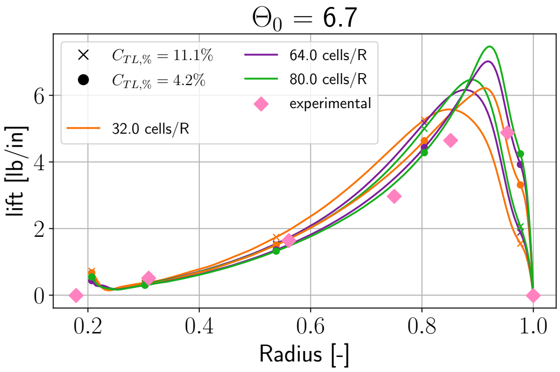

Fig. 20: Actuator line model with tip correction

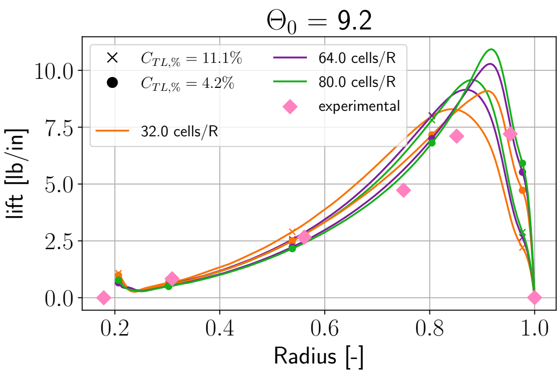

Fig. 21: Actuator line model with tip correction

B Appendix

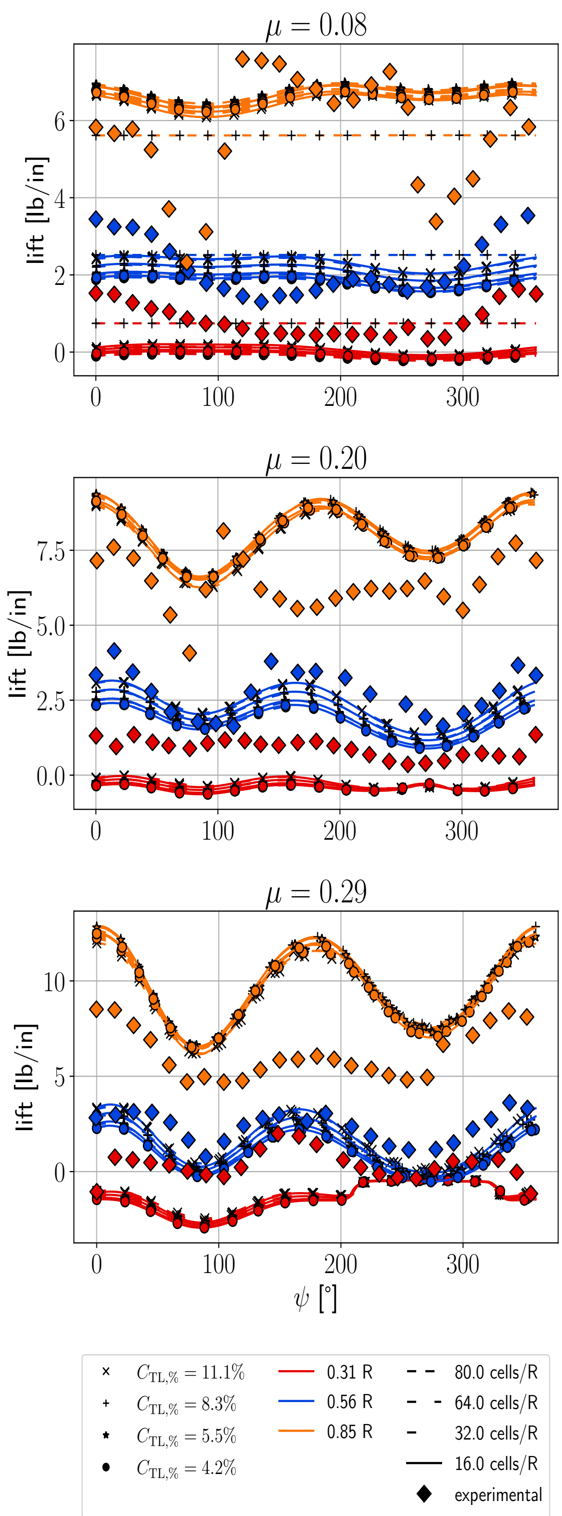

Fig. 22: Azimuth lift variation at two radial stations for different resolutions and tip loss for the linear-harmonic model.

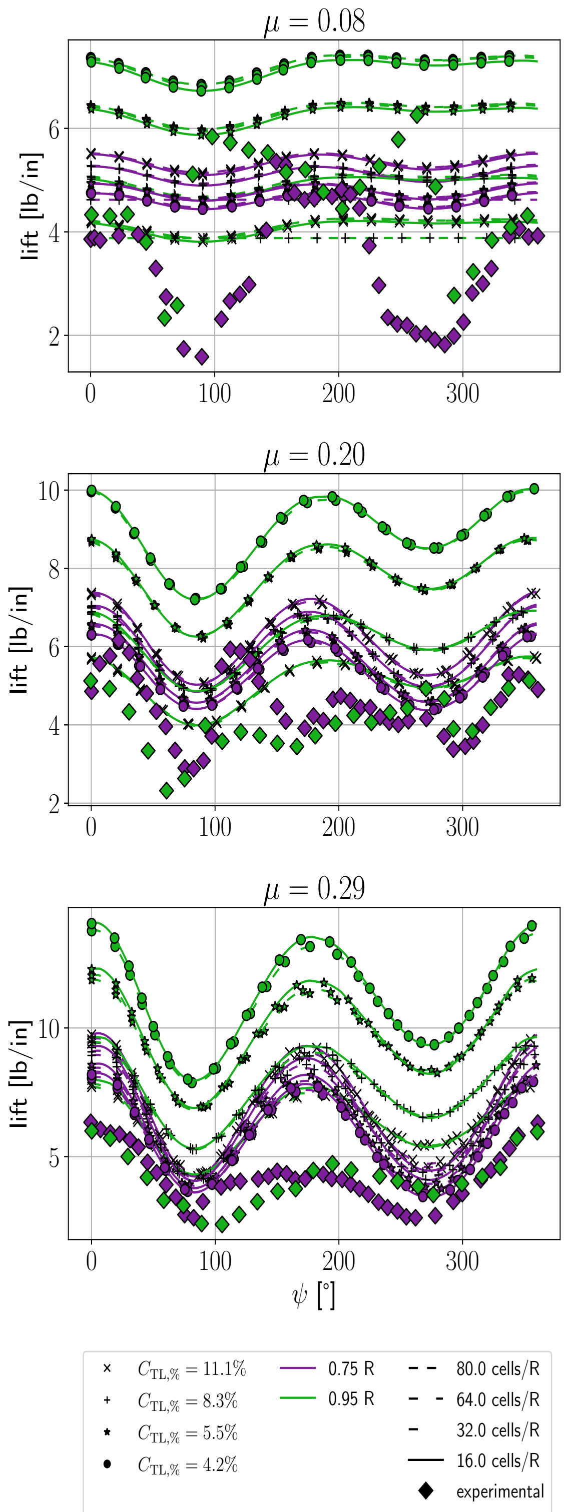

Fig. 23: Azimuth lift variation at three radial stations for different resolutions and tip loss for the linear-harmonic model.

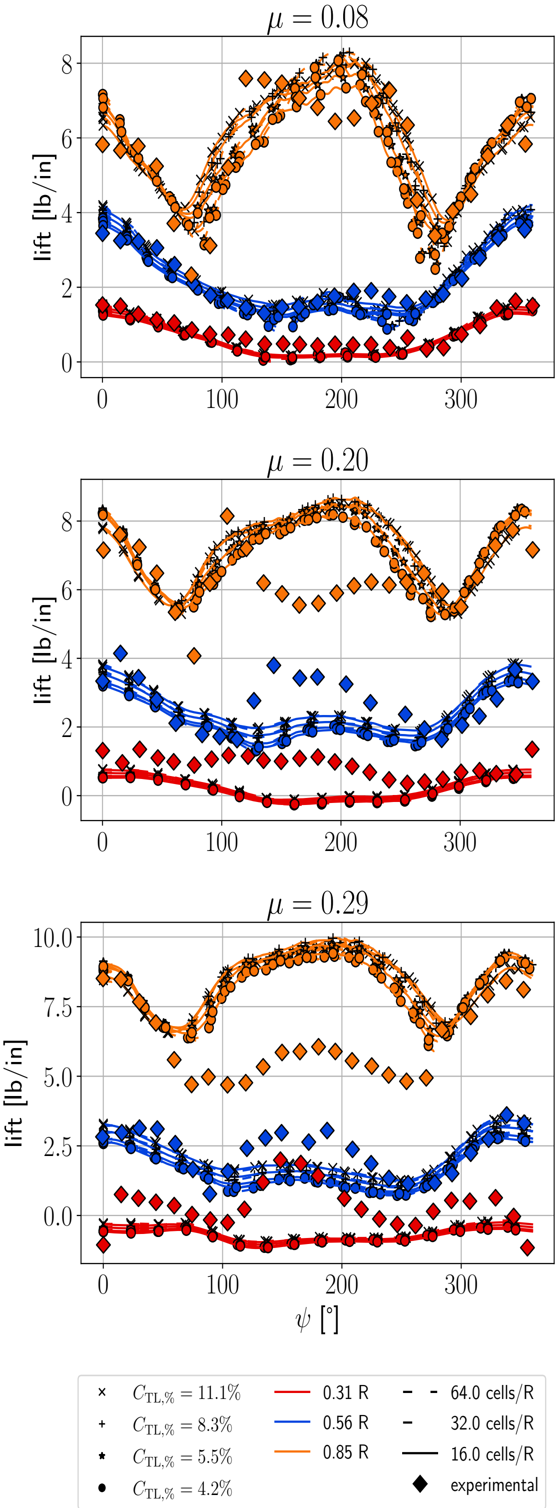

Fig. 24: Azimuth lift variation at two radial stations for different resolutions and tip loss for the Bessel-Fourier model.

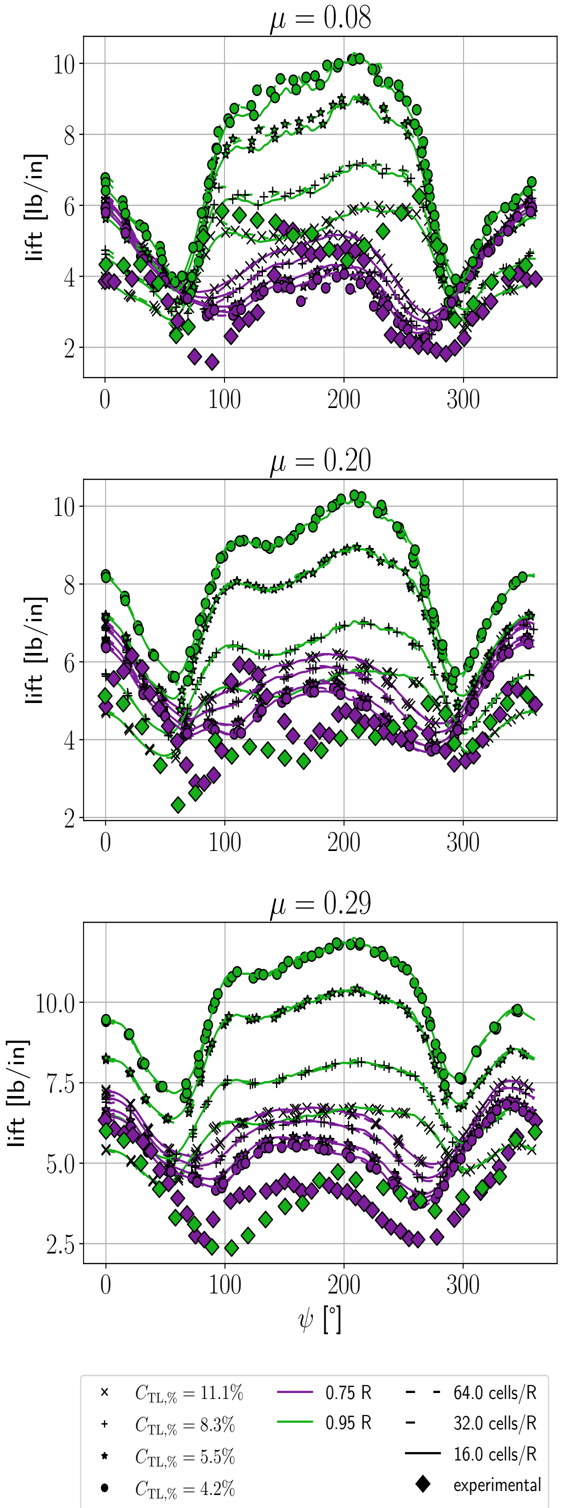

Fig. 25: Azimuth lift variation at three radial stations for different resolutions and tip loss for the Bessel-Fourier model.

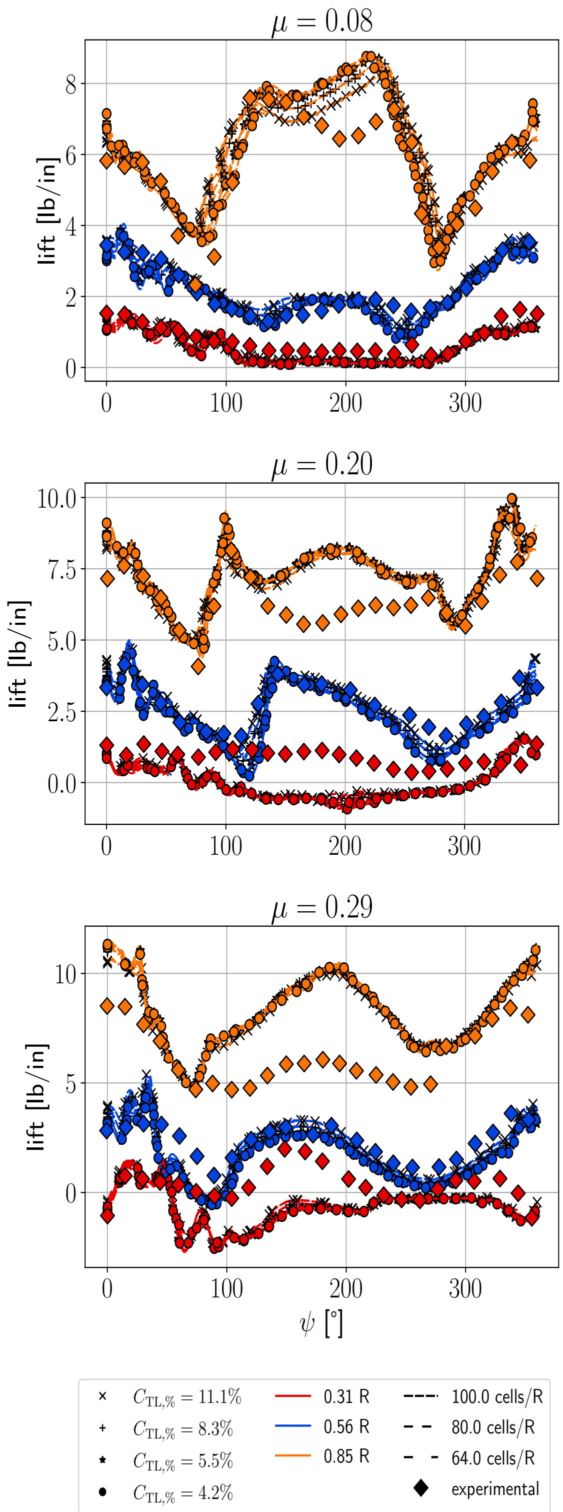

Fig. 26: Azimuth lift variation at two radial stations for different resolutions and tip loss for the actuator line model.

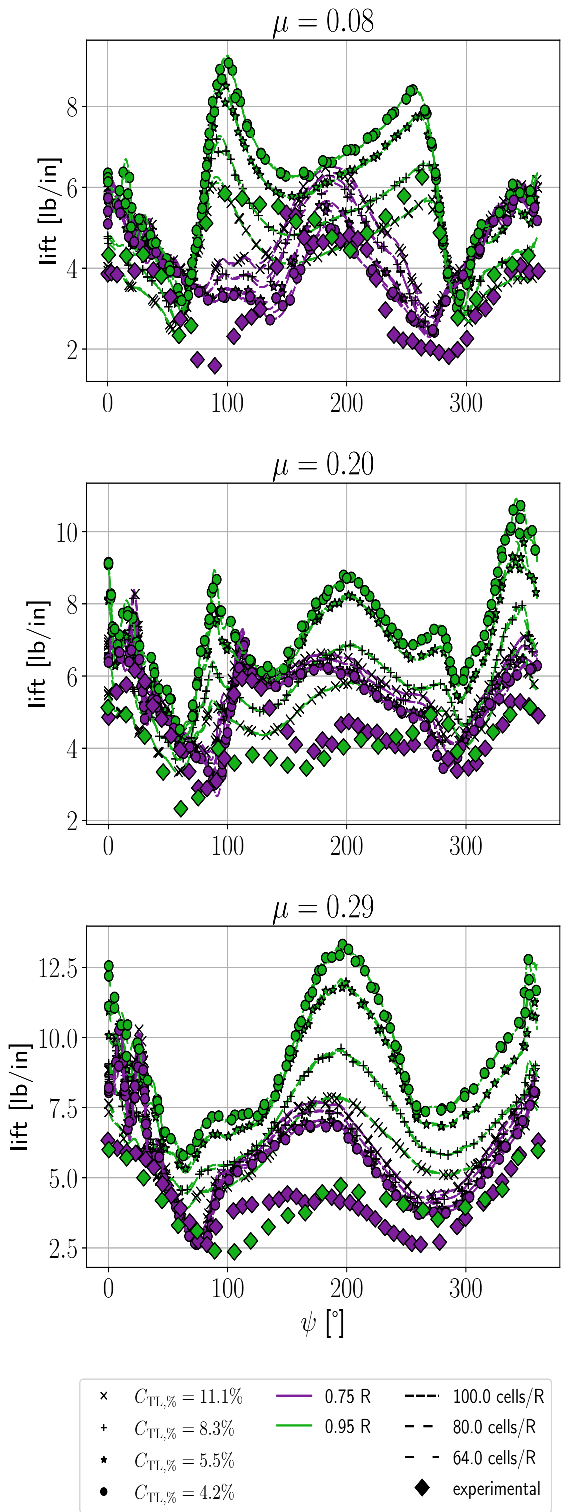

Fig. 27: Azimuth lift variation at three radial stations for different resolutions and tip loss for the actuator line model.

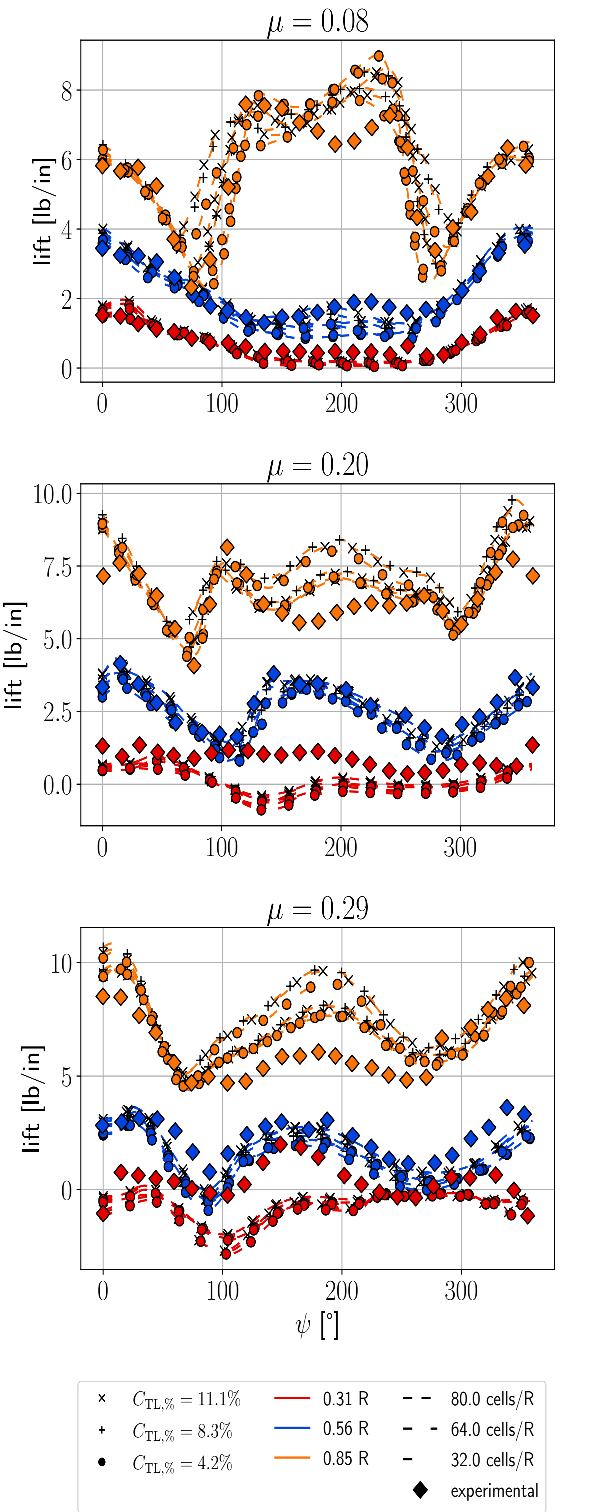

Fig. 28: Azimuth lift variation at two radial stations for different resolutions and tip loss for the actuator line model with the common kernel.

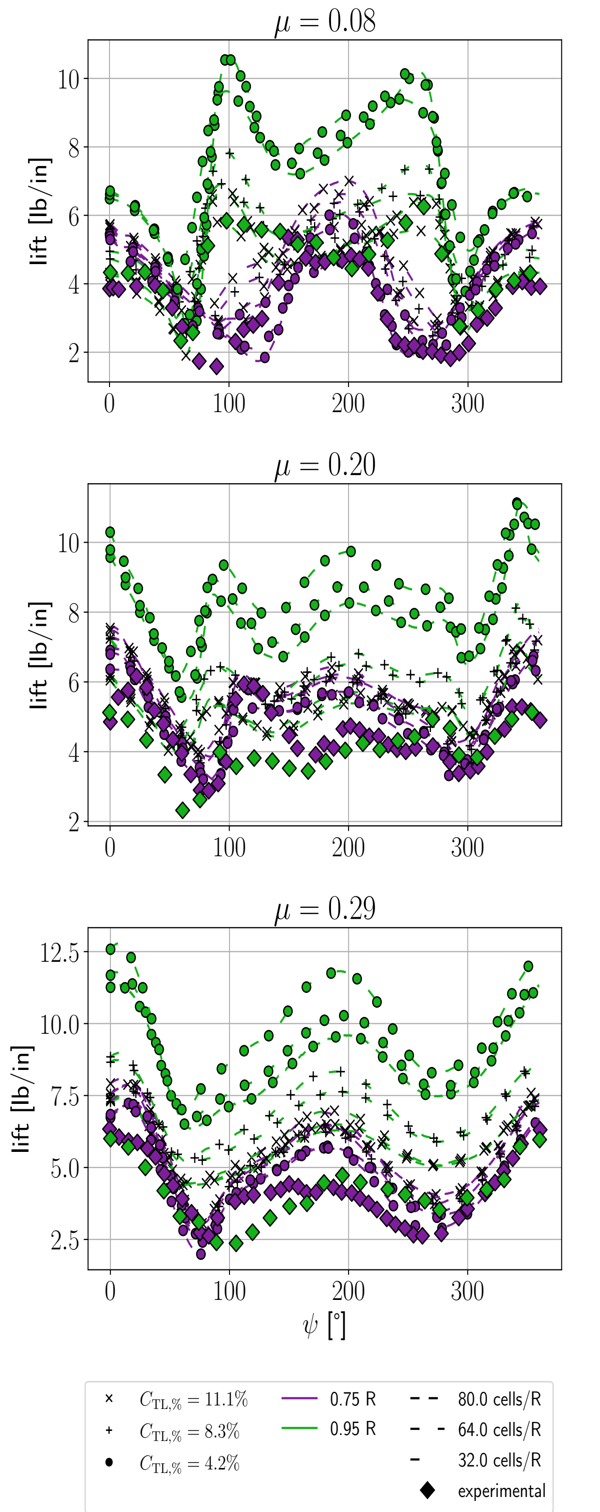

Fig. 29: Azimuth lift variation at three radial stations for different resolutions and tip loss for the actuator line model with the common kernel.

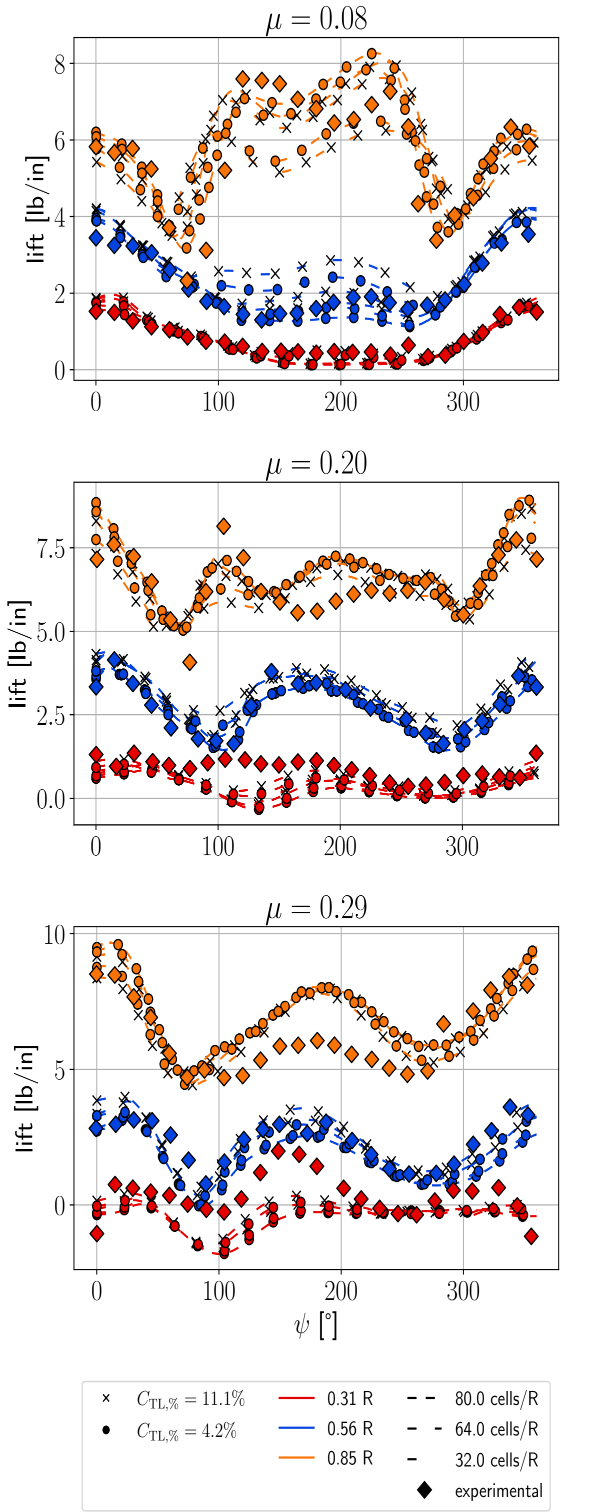

Fig. 30: Azimuth lift variation at two radial stations for different resolutions and tip loss for the actuator line model with tip correction.

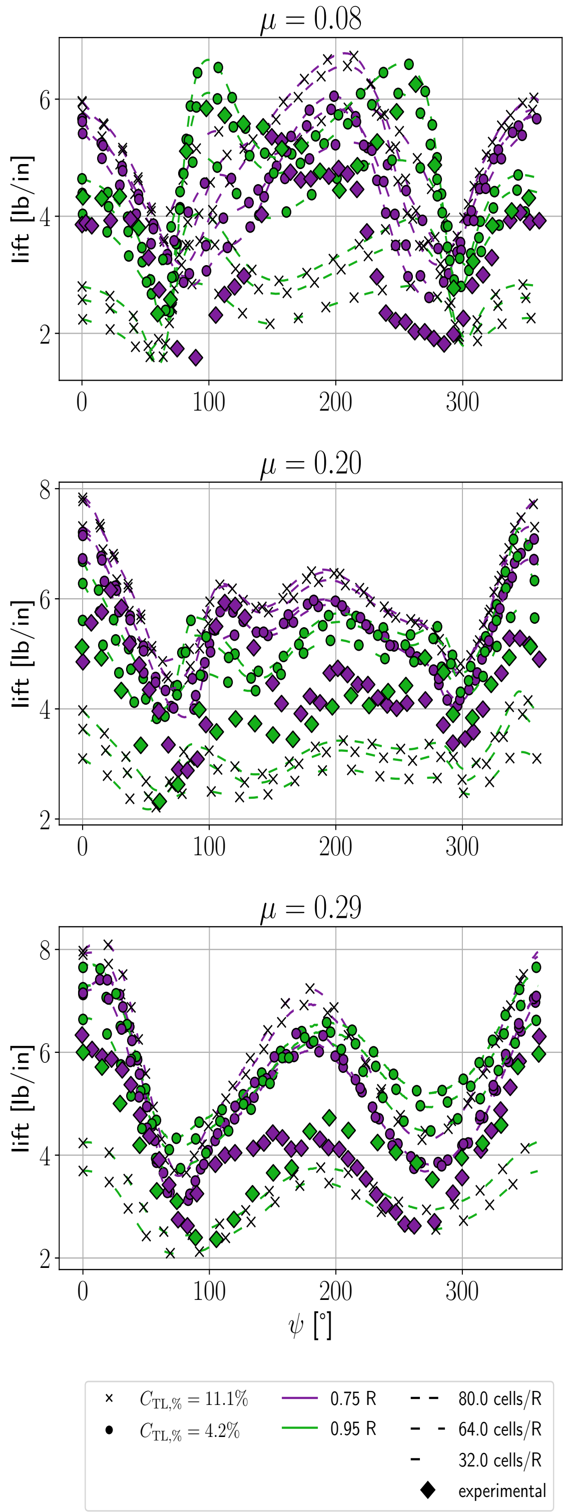

Fig. 31: Azimuth lift variation at three radial stations for different resolutions and tip loss for the actuator line model with tip correction.